Materials Advances

ROYAL SOCIETY OF CHEMISTRY

PAPER

View Article Online
View Journal

Cite this: DOI: 10.1039/d6ma00006a

Covalent triazine-capped Fe_3O_4 nanocomposites for efficient dye remediation: structural insights, adsorption mechanism, and recyclability

Shital R. Patel, *[a] Isha R. Patel, [b] Mehul S. Dave,[c] Nilkanth J. Faldu[d] and Tejas C. Sharma[e]

Received 5th January 2026,
Accepted 29th March 2026

DOI: 10.1039/d6ma00006a

rsc.li/materials-advances

The synthesis of covalent triazine frameworks (CTFs) conventionally requires a prolonged reaction time, particularly when prepared through nucleophilic substitution between 2,4,6-trichloro-1,3,5-triazine (TCT) and amino acid-based functional monomers. In this study, a Fe_3O_4-adn-(1,3,5-triazine-2,4,6-triyl)triproline nanocomposite was successfully synthesized and characterized using FT-IR spectroscopy, DSC, XRD, SEM and VSM analysis and TGA. The created substance demonstrated excellent adsorption proportion for the removal of hazardous industrial dyes, including Reactive Red 195 (RR-195), Reactive Blue 222 (RB-222), and Reactive Black 5 (RB-5). Batch adsorption studies at 10% (w/v) dye concentrations under alkaline conditions revealed high removal efficiencies of 95.8% (RR-195), 95.0% (RB-222), and 94.6% (RB-5) from real industrial effluents. Kinetic modeling indicates that the adsorption follows a pseudo-second-order mechanism, while isotherm analysis confirmed the suitability of the Langmuir adsorption model, suggesting monolayer adsorption. Reusability testing further showed that the adsorbent retained over 65% removal efficiency after ten successive cycles, establishing its potential as a sustainable, cost-effective and recyclable material for waste water treatment and dye remediation applications.

1. Introduction

Industrial wastewater is a substantial source of aquatic contamination, threatening both ecological equilibrium and human health. Among different type of industrial waste, printing and dyeing wastewater from the textile industry is particularly problematic due to its high chemical oxygen demand (COD), high concentration of hazardous organic compounds, and colors.[1–6] The textile dyeing sector generates wastewater which contains synthetic dyes, leading to increased pollution in the environment. Water that has been contaminated with dyes can irritate the eyes and skin when inhaled or touched. It is also linked to allergic reactions such as conjunctivitis, contact dermatitis, asthma and rhinitis. Research has shown that azo dyes can interfere with ovulation and sperm production, while reactive dyes may bind to human serum albumin, causing the body to make immunoglobulin E and release histamine. Azo dyes have been linked to cancer in organs such as the liver, bladder, and spleen, as well as chromosomal problems in mammalian cells.[7–12] Before releasing wastewater containing colors into water bodies, it is crucial for industries that employ dye to adequately clean it. This is because dye-contaminated wastewater poses serious threats to health and the environment (Scheme 1).

A diverse array of physicochemical and biological techniques have been employed to overcome wastewater contamination, including membrane filtration, flocculation, co-precipitation, photodegradation, and biological treatment. Among these strategies, adsorption onto porous materials has been widely recognized as one of the most effective methods owing to its high efficiency, low operation cost, simplicity, and environmental compatibility. The development of sustainable materials that offer an eco-friendly and cost-effective solution for the treatment of industrial wastewater and removal of hazardous organic pollutant has attracted descriminative interest in recent years due to an increase in environmental awareness and regulatory focus.[13–18]

The employment of magnetic particle technology for environmental remediation has attracted considerable research

[a] Department of Chemical Sciences, N. V. Patel College of Pure & Applied Science, Charutar Vidya Mandal University, Gujarat-388120, India. E-mail: shital28993@gmail.com
[b] Department of Organic Chemistry, Institute of Science & Technology for Advanced Studies & Research, Charutar Vidya Mandal University, Vallabh Vidyanagar, Anand, Gujarat 388120, India
[c] Department of Physics, N. V. Patel College of Pure & Applied Science, Charutar Vidya Mandal University, Gujarat-388120, India
[d] Department of Biological Sciences, N. V. Patel College of Pure & Applied Science, Charutar Vidya Mandal University, Gujarat-388120, India
[e] Department of Mathematical Sciences, N. V. Patel College of Pure & Applied Science, Charutar Vidya Mandal University, Gujarat-388120, India

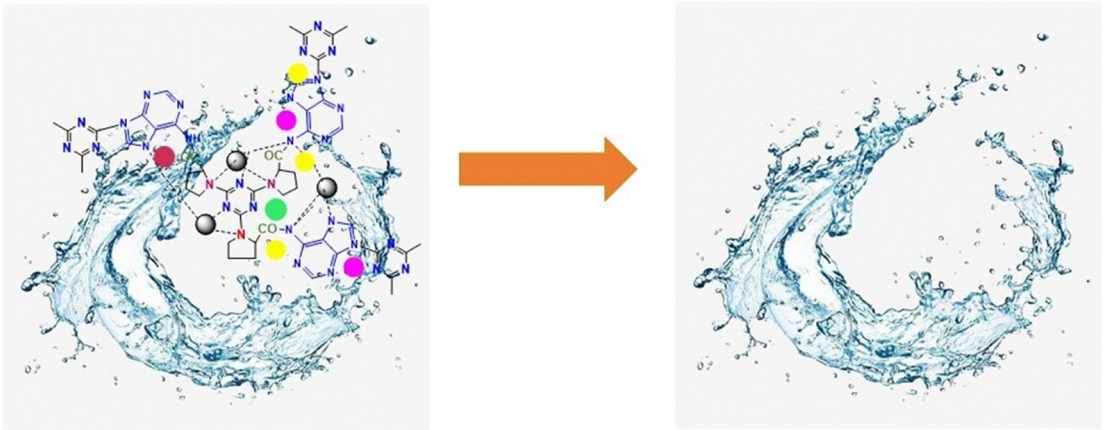

Scheme 1 A scheme showing the Fe_3O_4-adn-(1,3,5-triazine-2,4,6-triyl)triproline nanocomposite and its application in removing industrial organic dyes.

interest in recent years. Because they may be easily removed from aqueous solution using an external field, magnetic adsorbents offer a remarkable advantage that facilitates efficient recovery and repurposing. For the removal of dyes from wastewater, a variety of magnetic adsorbents such as magnetic nanoparticles, organic group modified chitosan, and magnetic Fe_3O_4 particles, have been developed and thoroughly investigated. The fabrication of these magnetic materials is often complex, involving multiple preparation steps and surface modifications; moreover, several of these materials have low surface areas, leading to limited adsorption capacities, thereby limiting their practical utility in large-scale wastewater treatment systems.[19–26]

2,4,6-Trichloro-1,3,5-triazine (TCT), also referred to as cyanuric chloride, is a significant heterocyclic chemical that structurally resembles aromatic benzene, with its carbon and nitrogen atoms. The electron-deficient triazine ring core has robust electron-accepting properties, facilitating diverse interactions with various contaminants. These features of TCT render it a promising candidate for the integration of functional polymers and hybrid materials with regenerative compatibilities, making it appropriate for applications in photocatalysis, adsorption, and environmental remediation.[27]

Surface functionalisation obliges as an admirable process to improve fussiness and customise surface properties for particular applications. An effective method to functionalize L-proline and adenine while preserving their intrinsic structural integrity is the assimilation of organic functional groups into the surface. One method for creating hybrid material is to modify L-proline and adenine with reactive functionalities that enable subsequent grafting of organic moieties. These functionalised systems validate improved kinship for dyes with both hydrophobic and hydrophilic groups, allowing the effective adsorptive removal of a prevalent array of contaminated for aquatic environments.[28–30]

To sum up, we successfully developed a covalently functionalised triazine-capped Fe_3O_4 nanocomposite that functions as an extremely effective magnetically recoverable adsorbent for removing reactive dyes from wastewater solutions. Numerous active sites that facilitate strong interaction, including π–π interactions, are introduced when nitrogen-rich triazine groups are incorporated onto the surface of Fe_3O_4.[31–34] The high adsorption capacity, rapid adsorption kinetics, and remarkable magnetic separability of this resultant nanocomposite enable effective adsorbent recovery and reuse without appreciable performance degradation over multiple cycles.[35–37] The advantages of the current material are due to direct covalent surface modification, which increases the availability of active sites and improves the adsorption efficiency when compared to previously reported magnetic triazine-based systems.[38] According to the results, magnetic nanocomposites functionalised with triazine provide a promising basis for developing recyclable adsorbents for wastewater treatment.[39]

This study aims to create a hybrid structure of L-proline, adenine, and magnetite nanoparticles with multifunctional capabilities through a strategic chemical design. The meticulous selection of organic components, emphasizing molecules having functional groups that may easily abbreviate with carboxylate function on L-proline surface and amino group on adenine. The adsorption efficacy of these materials was assessed using Reactive Red 195, Reactive Blue 222, and Reactive Black 5 dyes as representative industrial contaminants. Essential adsorption parameters were optimized, and the equilibrium data were evaluated utilising the Langmuir and Freundlich isotherm models, while the kinetics of the adsorption process were methodically scrutinized.

2. Experimental section

2.1. Materials and methods

Cyanuric chloride (*s*-triazine, Sigma-Aldrich), L-proline (Loba Chemie), adenine (Loba Chemie), potassium carbonate (Loba Chemie), and Fe_3O_4 nanoparticles with an average particle size of around 50–100 nm (Sigma-Aldrich) were used without further purification. We also collected the industrial effluent from Meghmani dyes and intermediates Ltd, located in Ahmedabad, Gujarat. The sample was a mixture of three dyes: Reactive Red (RR-195), Reactive Blue 222 (RB-222) and Reactive Black 5 (RB-5). The chemical structure and characteristics of the dyes are shown in Fig. 1. All testing method was conducted by using

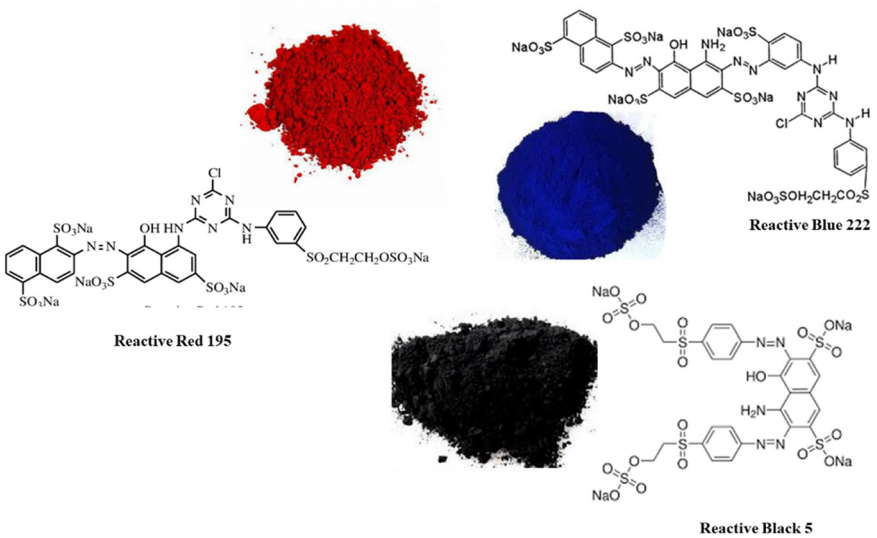

Fig. 1 Characteristics of Reactive Red 195 (RR-195), Reactive Blue 222 (RB-222) and Reactive Black 5 (RB-5) dyes.

ultrapure double-distilled water to guarantee the elimination of contaminants.

2.2. Instrument and characterization

The synthesized Fe_3O_4-adn-(1,3,5-triazine-2,4,6-triyl)triproline nanocomposite was characterized to confirm its chemical structure and thermal stability. The characterization of the synthesized material was carried out using various analytical techniques, including Fourier transform infrared (FTIR) spectroscopy (PerkinElmer, USA), X-ray diffraction (XRD) analysis (Bruker D8 Advance, Cu target X-ray tube, X-ray power: 2 kW, detector: LYNXEYE XE-T, and scanning range: 2° to 136°), thermogravimetric analysis (TGA) (PerkinElmer-4000, USA), and differential scanning calorimetry (DSC) (PerkinElmer-800, USA). N_2 adsorption–desorption isotherm was obtained using a Micrometrics 3Flex Analyser and Smart Vac Degasser to determine the surface area and pore volumes. Additionally, a UV-vis spectrophotometer (UV/vis 160A, Shimadzu, Japan) was used for spectroscopic analysis.

2.3. Dye adsorption studies

The adsorption experiments were conducted under controlled conditions to ensure reproducibility and accurate evaluation of the adsorption performance. Batch adsorption studies were carried out at 25 ± 2 °C with continuous agitation at 150 rpm using an orbital shaker in order to maintain a uniform dispersion of the adsorbent and enhance mass transfer between the dye molecules and adsorption sites. The equilibrium time was set at 60 minutes based on preliminary kinetic experiments that demonstrated that adsorption equilibrium reached within this time. A 10% (w/v) dye concentration was selected to mimic the relatively high dye loading conditions frequently found in industrial textile effluents in order to evaluate the adsorption capacity and efficacy of the triazine-capped Fe_3O_4 nanocomposite under realistic wastewater scenarios. The adsorption performance of the Fe_3O_4-adn-(1,3,5-triazine-2,4,6-triyl)triproline nanocomposite toward Reactive Red 195 (RR-195), Reactive Blue 222 (RB-222) and Reactive Black 5 (RB-5) was evaluated using batch experiments.

The adsorption kinetic experiments were carried out in a 50 mL dye effluent solution at room temperature. The synthesized material was used as an adsorbent at a dosage of about 25 mg and added to the Reactive Red (RR-195) dye solutions with a concentration of 300 mg L^{-1}. The effects of solution pH, treatment time, adsorbent dosage and initial dye concentration[1–6] on adsorption were systematically evaluated in separate experiments. After equilibrium, the solutions were analysed. The adsorption capacity and % dye removal were calculated using the following equations.

$$q_e = (C_0 - C_e)V/m \quad (1)$$

where C_0 and C_e (mg L^{-1}) are the initial and equilibrium concentrations of the dyes, respectively; V (L) is the volume of the dye solution; and m (g) is the mass of the synthesized material.

$$R\ (\%) = (C_0 - C/C_0) \times 100 \quad (2)$$

where C_0 is the initial concentration of the dye, C is the equilibrium concentration, V is the volume of the solution, and m is the mass of the adsorbate.

3. Results and discussion

3.1. Synthesis of (4,6-dichloro-1,3,5-triazin-2-yl)proline

A mixture of cyanuric chloride (18.44 g, 0.1 mol) in acetone was agitated with an aqueous sodium bicarbonate solution (8.40 g in 100 mL of distilled water) at 0–5 °C for 2 hours. A solution of L-proline (11.51 g, 0.1 mol) was added dropwise to the cooled reaction mixture while maintaining continuous stirring. The reaction was maintained at a constant temperature for an additional 3 hours to ensure complete substitution. The resultant solid precipitate was filtered, meticulously rinsed with distilled water, and dried. The crude product was subsequently recrystallized from ethanol to provide the purified L-proline-substituted cyanuric chloride derivative.

3.2. Synthesis of (1,3,5-triazine-2,4,6-triyl)triproline

A solution of (4,6-dichloro-1,3,5-triazin-2-yl)L-proline (26.03 g, 0.1 mol) in 40 mL of acetone was incrementally added to a stirred mixture of sodium hydroxide (16 g, 0.4 mol) and L-proline (23.03 g, 0.2 mol) at ambient temperature. The reaction mixture was agitated constantly for 3 hours, then refluxed at 80 °C for an additional 3 hours to ensure complete condensation. Upon completion of the reaction, the resultant precipitate was collected *via* filtration, meticulously washed with distilled water, and dried. The crude product was purified *via* recrystallization from acetone to provide the required compound. The Fujiwara test revealed the absence of unreacted dichloro-*s*-triazine, confirming the effective substitution and the purity of the final product.

3.3. Synthesis of the Fe_3O_4-adn-(1,3,5-triazine-2,4,6-triyl)triproline nanocomposite

To synthesize the triazine-modified magnetic polymeric networks, activated Fe_3O_4 (0.50 g) was initially dispersed in *N*,*N*-dimethylformamide (DMF, 50 mL) and sonicated for 1 hour to get a homogenous suspension. Subsequently, 37.84 g of (1,3,5-triazine-2,4,6-triyl)triproline was incorporated into the stirred mixture of sodium hydroxide and adenine (13.51 g, 0.1 mol), and the reaction mixture was refluxed for 48 hours with constant agitation. Upon completion, the black solid product was magnetically separated, meticulously cleaned with ethanol and deionized water, and subsequently dried at ambient temperature. Fig. 2. presents a schematic of the preparation of Fe_3O_4-adn-(1,3,5-triazine-2,4,6-triyl)triproline nanocomposite.

3.4. Fourier transform infrared (FTIR) spectroscopy

3.4.1. FTIR of (4,6-dichloro-1,3,5-triazin-2-yl)proline. The FTIR (Fig. 3A) spectrum of (4,6-dichloro-1,3,5-triazin-2-yl)proline exhibited a wide band at 3157–3070 cm^{-1} indicative of O–H/N–H stretching vibrations. A prominent peak at 1674 cm^{-1} was attributed to the C═O stretching of the proline unit, while the bands between 1624 and 1574 cm^{-1} were ascribed to $–CH_2$ and C–N vibrations, and the range of 845–700 cm^{-1} exhibited distinctive C–Cl stretching, corroborating the synthesis of the intended triazine-proline derivative.

3.4.2. FTIR of (1,3,5-triazine-2,4,6-triyl)triproline. The FTIR (Fig. 3B) spectrum of (1,3,5-triazine-2,4,6-triyl)triproline show

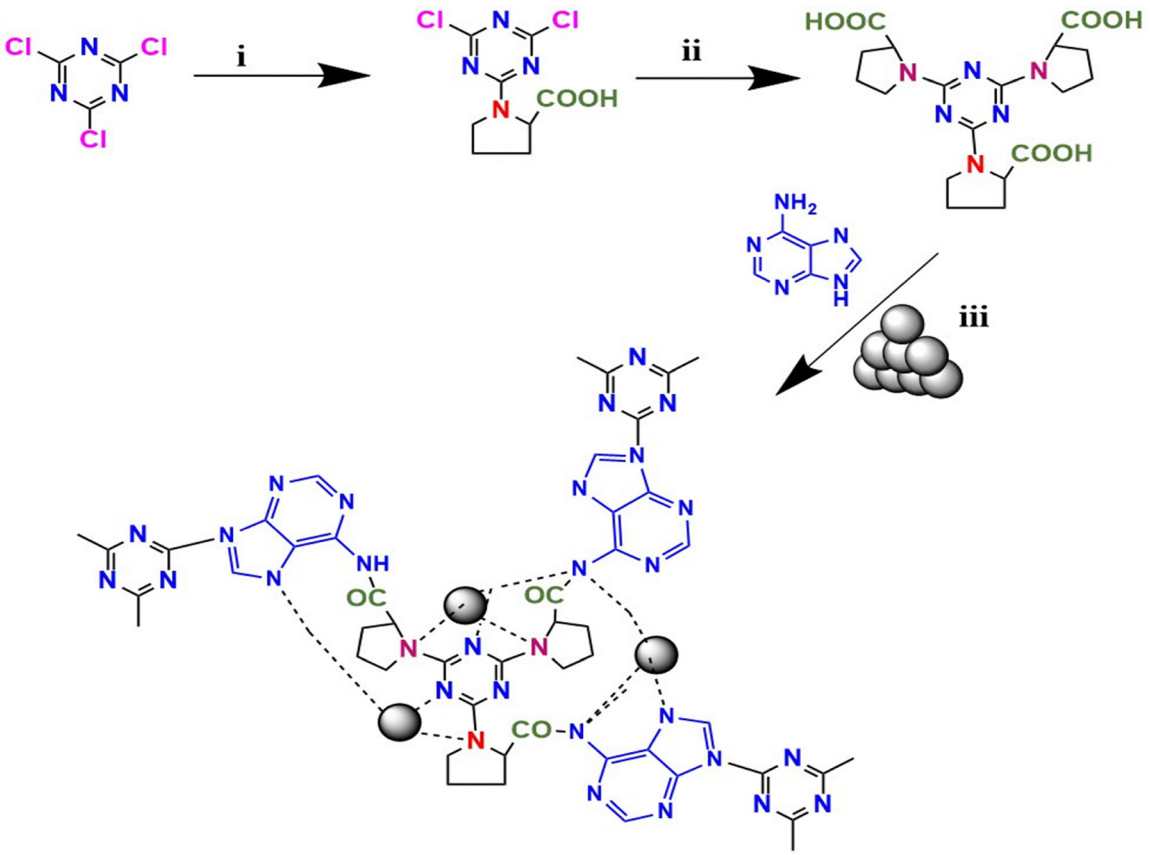

Scheme-1 Synthetic route of Triazine-Modified Magnetic Polymeric Networks
Reagent and conditions: (i) $NaHCO_3$, Acetone, 0–5°C, 2 h
(ii) NaOH, acetone, RT, 3 h, further stir at 80°C, 3 h
(iii) Fe_3O_4, Adenine, DMF, 170–190 °C, 8 h

Fig. 2 Plausible reaction scheme and the structure of the Fe_3O_4-adn-(1,3,5-triazine-2,4,6-triyl)triproline nanocomposite.

large absorptions at 3080–2924 cm^{-1}, attributed to O–H and N–H stretching vibrations. The prominent bands at 1751 and 1710 cm^{-1} are indicative of C═O stretching, whereas the peaks in the range of 1593–1508 cm^{-1} are attributed to C–N and CH_2 vibrations, and the bands at 833–542 cm^{-1} validate triazine ring deformation and skeletal modes. These characteristics simplify the formation of the triazine-proline network.

3.4.3. FTIR of the Fe_3O_4-adn-(1,3,5-triazzine-2,4,6-triyl)triproline nanocomposite. The FTIR (Fig. 3C) spectrum of the Fe_3O_4-adn-(1,3,5-triazine-2,4,6-triyl)triproline nanocomposite has a wide band at 3209–3053 cm^{-1}, ascribed to the overlapping O–H/N–H stretching of adenine and proline, alongside aliphatic C–H bands at 2885 and 2833 cm^{-1}. Intense adsorption at 1776–1714 cm^{-1} and 1061–1051 cm^{-1} corresponds to the C–N/C═C skeleton and C–N/C–O stretching vibrations, respectively. The peaks at 842–763 cm^{-1} are ascribed to vibrations of the triazine/adenine ring. The distinctive Fe–O stretching bands at 540, 447 and 419 cm^{-1} validate the presence of the magnetite core and effective organic capping.

3.4.4. FTIR of the regenerated Fe_3O_4-adn-(1,3,5-triazzine-2,4,6-triyl)triproline nanocomposite. FTIR spectroscopy (Fig. 3D) was used to assess the structural stability of the Fe_3O_4-adn-(1,3,5-triazine-2,4,6-triyl)triproline nanocomposite following adsorption–desorption cycles. The spectrum demonstrates that the regenerated material maintained the distinctive vibrational bands seen in the new adsorbent. Aromatic C–H stretching is represented by the bands at 3094 cm^{-1}, whereas aliphatic C–H vibrations are represented by the bands at 2924 and 2852 cm^{-1}. The triazine ring C═N stretching is responsible for the prominent peak at 1665 cm^{-1}, while aromatic ring vibrations are represented by the bands at 1598–1556 cm^{-1}. The bands at 1209–1035 cm^{-1} show C–N/C–O vibrations, while the peaks at 1444–1354 cm^{-1} are the result of C–N stretching. The preservation of the Fe_3O_4 core is confirmed by the Fe–O stretching band in the low-frequency region. The significant shift in peak locations shows that the chemical framework is unaltered following recycling.

3.5. Differential scanning calorimetry (DSC)

3.5.1. DSC of the Fe_3O_4-adn-(1,3,5-triazine-2,4,6-triyl)triproline nanocomposite. The DSC thermogram (Fig. 4A) of the Fe_3O_4-adn-(1,3,5-triazine-2,4,6-triyl)triproline nanocomposite displays several temperature changes, indicating the intricate structure of the hybrid nanocomposite. The slight endothermic variation noted below 120 °C is attributed to the release of absorbed or loosely bound moisture. Distinct glass transition events observed at 189–196 °C and 270–282 °C are ascribed to the segmental relaxation of the adenine and triazine proline moieties, respectively, within the polymeric shell. The extensive exothermic shift over 300 °C, succeeded by a significant thermal event at 493–506 °C, signifies ongoing structural reorganization, crosslinking, and subsequent breakdown of the organic matrix. At high temperatures validates the significant thermal stability and robust interfacial interaction between the Fe_3O_4 core and the organic triazine-adenine-proline framework.

3.5.2. DSC of the dye-absorbed Fe_3O_4-adn-(1,3,5-triazine-2,4,6-triyl)triproline nanocomposite. The DSC thermogram

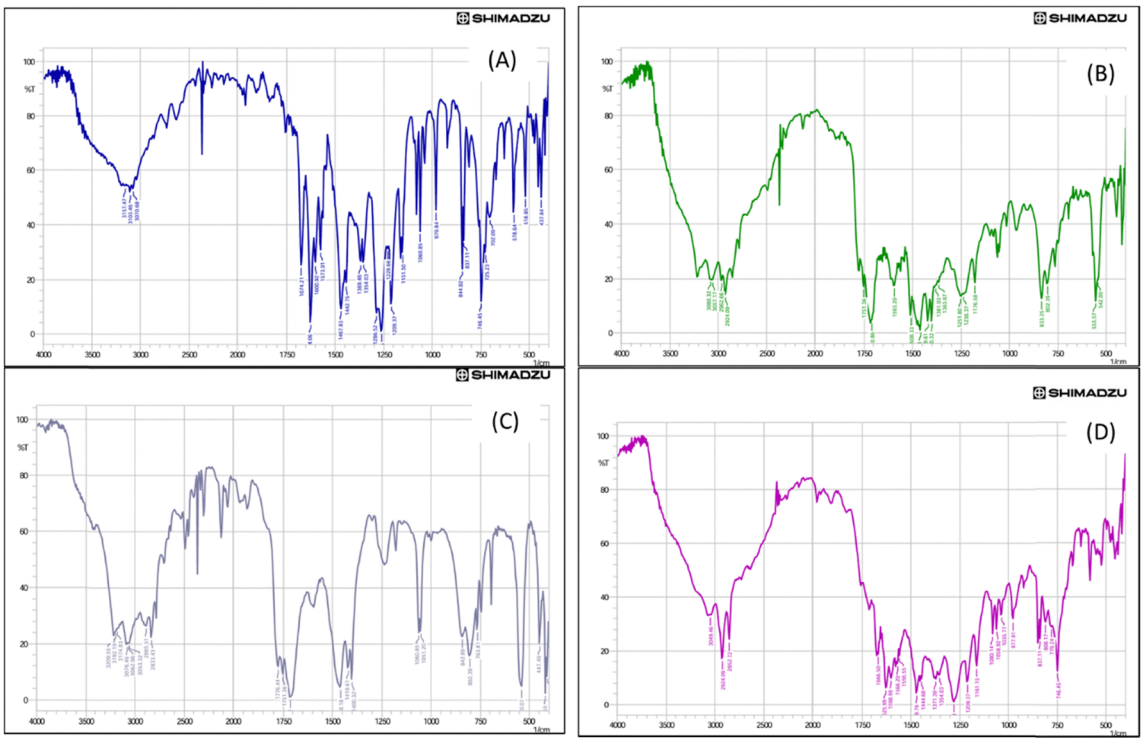

Fig. 3 FTIR spectra of (4,6-dichloro-1,3,5-triazin-2-yl)proline (A), (1,3,5-triazine-2,4,6-triyl)triproline (B) and the Fe_3O_4-adn-(1,3,5-triazine-2,4,6-triyl)triproline nanocomposite (C) and the regenerated Fe_3O_4-adn-(1,3,5-triazine-2,4,6-triyl)triproline nanocomposite after adsorption–desorption cycles (D).

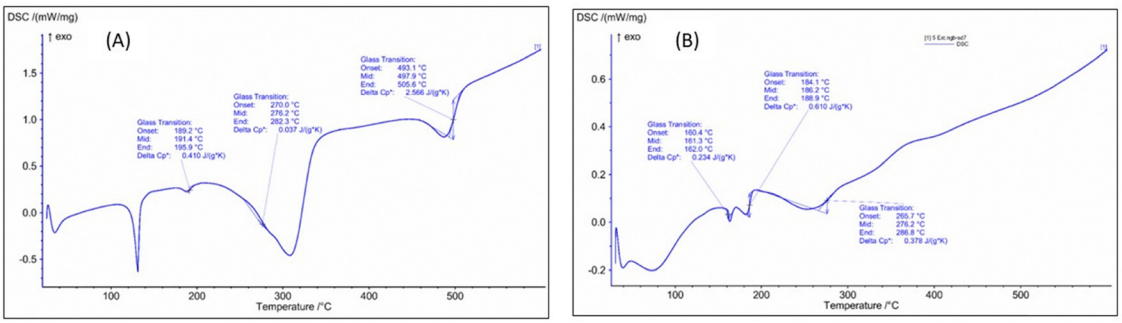

Fig. 4 DSC of the Fe_3O_4-adn-(1,3,5-triazine-2,4,6-triyl)triproline nanocomposite (A) and the RR-195 dye-adsorbed Fe_3O_4-adn-(1,3,5-triazine-2,4,6-triyl)triproline nanocomposite (B).

(Fig. 4B) of the dye-adsorbed Fe_3O_4-adn-(1,3,5-triazine-2,4,6-triyl)triproline nanocomposite exhibits remarkable multi-step thermal changes, signifying structural alteration following dye adsorption. The earliest endothermic phenomenon occurring below 120 °C is related to the desorption of physically absorbed moisture or solvent remnants. Three distinct glass transition regions are identified at 160–162 °C, 184–189 °C, and 265–287 °C, with the corresponding C_p values of 0.234, 0.610, and 0.378 J g^{-1} K^{-1}, respectively. The lower-temperature transitions are ascribed to localized molecular relaxations within the adenine and triazine-proline domains, whereas the higher-temperature T_g indicates constrained segmental motion resulting from robust interfacial interaction among the Fe_3O_4 core, organic matrix, and adsorbed dye molecules. The absence of a significant degradation exotherm below 400 °C suggests that the hybrid nanocomposite preserves its thermal integrity following dye adsorption. The DSC profile indicates that the dye adsorption improves the molecular packing and thermal rigidity in the Fe_3O_4-adn-(1,3,5-triazine-2,4,6-triyl)triproline nanocomposite network.

3.6. Thermogravimetric analysis (TGA)

3.6.1. TGA of the Fe_3O_4-adn-(1,3,5-triazine-2,4,6-triyl)triproline nanocomposite. The TGA curve (Fig. 5A) of the Fe_3O_4-adn-(1,3,5-triazine-2,4,6-triyl)triproline nanocomposite displays two significant stages of weight reduction. The initial substantial loss of around 70.5% within the temperature range of 50–320 °C is attributed to the elimination of physically absorbed water and the degradation of surface-attached chemical groups, including adenine, triazine, and proline moieties. The second stage, accounting for roughly 27.4% between 350 and 500 °C, is ascribed to the breakdown of the residual organic matrix covalently bonded to the Fe_3O_4 surface. Above 500 °C, the mass remains relatively unchanged, signifying the formation of a thermally stable Fe_3O_4 residue. The results validate the effective capping of Fe_3O_4 nanoparticles with the organic triazine-adenine-proline framework, resulting in improved thermal stability.

3.6.2. TGA of the dye-adsorbed Fe_3O_4-adn-(1,3,5-triazine-2,4,6-triyl)triproline nanocomposite. The TGA (Fig. 5B) profile of the dye-adsorbed Fe_3O_4-adn-(1,3,5-triazine-2,4,6-triyl)triproline nanocomposite reveals three discrete stages of weight loss. The preliminary 3.8% reduction below 140 °C is ascribed to the elimination of physically adsorbed water and moisture. The principal decomposition phase of approximately 39.5% occurring between 200 and 350 °C pertains to the thermal degradation of the organic coating, encompassing adenine, triazine, proline linkages, and the adsorbed dye molecules. An additional 8.2% loss between 400 and 500 °C results from the degradation of tightly bound residual organic constituents and dye fragments.

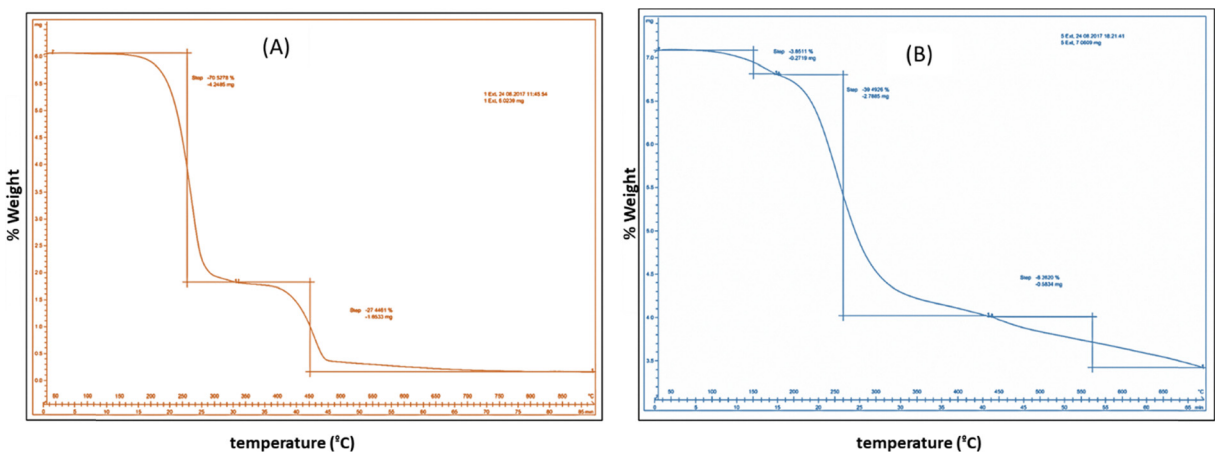

Fig. 5 TGA curves of the Fe_3O_4-adn-(1,3,5-triazine-2,4,6-triyl)triproline nanocomposite (A) and the RR-195 dye-adsorbed Fe_3O_4-adn-(1,3,5-triazine-2,4,6-triyl)triproline nanocomposite (B).

Above 550 °C, the curves stabilize, signifying the existence of a thermally stable Fe_3O_4 residue. This thermal pattern validates the effective dye adsorption and robust stability of the organic–inorganic hybrid nanocomposite.

3.7. XRD of the Fe_3O_4-adn-(1,3,5-triazine-2,4,6-triyl)triproline nanocomposite

The XRD (Fig. 6) pattern of the Fe_3O_4-adn-(1,3,5-triazine-2,4,6-triyl)triproline nanocomposite exhibits distinct diffraction peaks at $2\theta \approx 30.2^\circ$, 35.5°, 43.2°, 53.6°, 57.1°, and 62.7°, which correspond to the (220), (311), (400), (422), (551), and (440) planes, respectively, of the cubic inverse spinal Fe_3O_4 (JCPDS no. 19-0629). The lack of contaminant phases verifies the phase purity of magnetite. A diffuse broad background in the 15°–30° range is ascribed to the amorphous organic capping layer. The persistence of Fe_3O_4 diffraction peaks post-functionalization signifies effective surface capping without modification of the crystalline structure, validating the creation of the Fe_3O_4 based organic–inorganic composite.

3.8. Vibrating sample magnetometer (VSM)

The VSM hysteresis loop (Fig. 7) of the Fe_3O_4-adn-(1,3,5-triazine-2,4,6-triyl)triproline nanocomposite displays an S-shaped curve with little coercivity ($H_c < 50$ Oe) and exceedingly low remanence, indicating super magnetic characteristics at ambient temperature. The saturation magnetisation ($M_s \approx 0.26$ emu) is inferior to that of bare Fe_3O_4, which is ascribed to the existence of the non-magnetic triazine-triproline capping layer. Nonetheless, the composite preserves adequate magnetic responsiveness, facilitating effective magnetic separation while upholding surface functionalization.

3.9. Brunauer–Emmett–Teller analysis

The observed adsorption performance of the materials is highly correlated with their textural properties obtained from BJH and BET analyses (Fig. 8). With a well-defined mesoporous structure (~20 Å) and a higher specific surface area (~80–220 $m^2\ g^{-1}$),

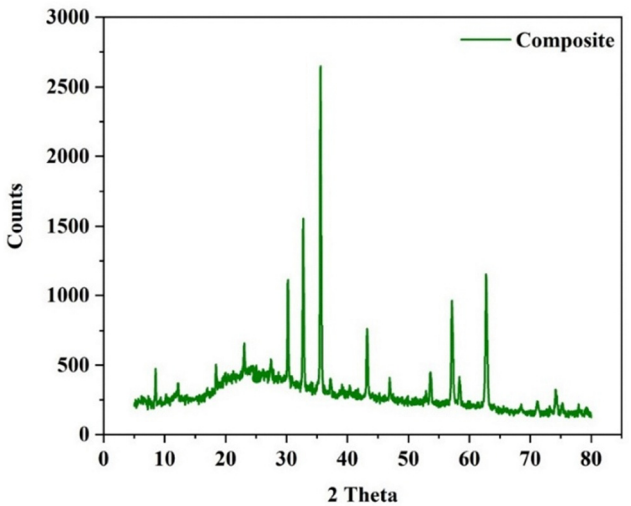

Fig. 6 XRD patterns of the Fe_3O_4-adn-(1,3,5-triazine-2,4,6-triyl)triproline nanocomposite.

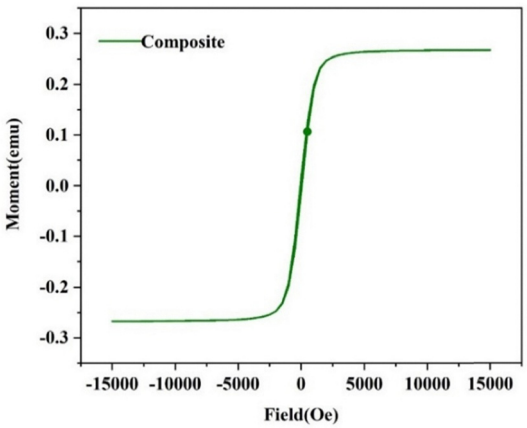

Fig. 7 Magnetic hysteresis curve of the Fe_3O_4-adn-(1,3,5-triazine-2,4,6-triyl)triproline nanocomposite.

the binder-less sample offers more accessible active sites, which directly contributes to its higher adsorption capacity (q_e) compared to that of the Fe_3O_4-adn-(1,3,5-triazine-2,4,6-triyl)triproline nanocomposite. The mass transfer resistance is reduced by the enhanced pore volume and homogeneous mesopore distribution, which promote effective dye molecule diffusion into the internal pore network.

From a kinetic standpoint, the increased mesoporosity of the Fe_3O_4-adn-(1,3,5-triazine-2,4,6-triyl)triproline nanocomposite facilitates faster adsorption rates, which are in line with the pseudo-second-order kinetic model and suggest that chemisorption involving surface functional groups is important. Furthermore, by enhancing interparticle diffusion, the existence of mesopores facilitates quick equilibrium attainment. The superior surface properties of the nanocomposite favor monolayer adsorption behaviour in terms of adsorption isotherms, as shown by a better fit to the Langmuir isotherms, indicating a homogeneous distribution of active sites. Fe_3O_4-adn-(1,3,5-triazine-2,4,6-triyl)triproline nanocomposite has a comparatively smaller surface area and pore volume, leading to slower kinetics and decreased adsorption capacity, underscoring the crucial role of textural characteristics. Overall, the combined BJH-BET and adsorption analyses show that the binder-free material improved mesoporosity and surface area, which are important factors controlling its enhanced adsorption efficiency, favorable kinetics, and strong isotherm behaviour, confirming its potential as an effective adsorbent for dye removal applications.

3.10. Optimization of the dye removal performance data

Optimization is a very important part of every analytical procedure since it makes the approach more sensitive and accurate in different situations. By fine-tuning the parameters, it helps the system operate at its best while still being able to handle the intricacies and variability of real-world samples.

3.10.1. Effect of pH. Fig. 9 illustrates the impact of pH removal efficiency of the dyes RR-195, RB-222, and RB-5. Dye removal was notably elevated under alkaline conditions, especially

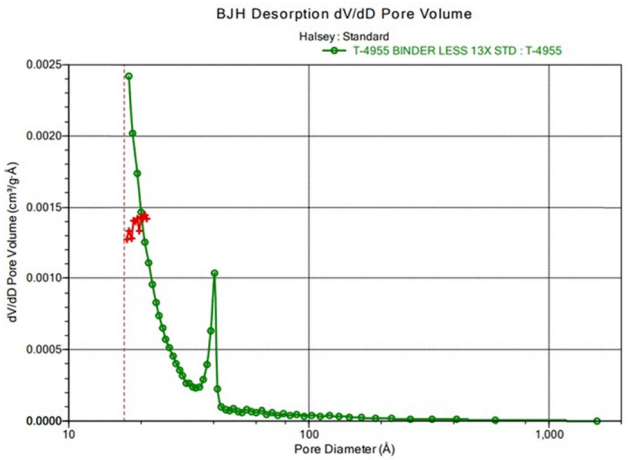

Fig. 8 BJH desorption pore size distribution (d*V*/d*D* *vs.* pore diameter) of the synthesized sample calculated using the Hasley standard model.

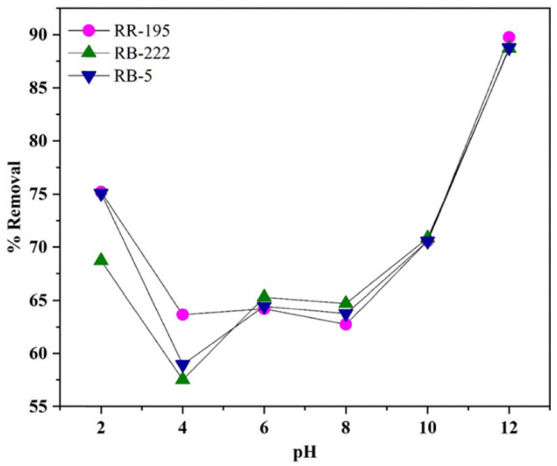

Fig. 9 Effect of pH on % dye removal of RR-195, RB-222 and RB-5 dyes by the Fe_3O_4-adn-(1,3,5-triazine-2,4,6-triyl)triproline nanocomposite (adsorbent dose = 10 mg, solution volume = 50 mL, solid–liquid ratio = 0.2 g L^{-1}, and temperature = 298 K).

for RR-195 and RB-5, owing to the protonation of surface functional groups that intensifies electrostatic attraction with reactive dye molecules. A reduction in the removal effectiveness was noted in the pH range, attributable to the diminished surface charge density and weaker dye-adsorbent interactions. At alkaline pH, the removal efficiency for all dyes markedly increased, attaining peak values at pH 12 (about 90% for RR-195, approximately 89% for RB-5, and approximately 88% for RB-222). The increase correlates with the high ionization of functional groups on the adsorbent surface, facilitating stronger interactions with dye molecules. The consistently elevated removal of RR-195 indicates its strong affinity for the adsorbent. Low standard deviation values (SD < 1%) signify excellent experimental repeatability.

Zeta potential measurements were assessed over a pH range of 2–12 in order to comprehend the surface charge behaviour of the synthesized triazine-functionalised Fe_3O_4 nanocomposite, as it regulates the electrostatic interactions between the adsorption of reactive dyes. The findings show that the zeta potential gradually decreases with increasing pH, shifting from positive values in acidic environments to negative values in alkaline conditions. The point of zero charge (pHpzc) of the triazine-functionalised Fe_3O_4 nanocomposite is found to be pH 6–7. The protonation of nitrogen-containing functional groups in the triazine ring causes the adsorbent surface to become positively charged at pH values below pHpzc. This increases the electrostatic attraction between the negatively charged sulfonate groups of the reactive dyes (RR-195, RB-222 and RB-5) and the positively charged adsorbent surface. A negatively charged adsorbent surface is produced when the pH rises above the pHpzc due to the protonation of surface functional groups. Adsorption may occur in this region *via* hydrogen bonding interactions with surface functional groups and π–π interactions between the aromatic structures of dye molecules and the triazine rings. These findings confirm that the pH-dependent adsorption behavior shown in Fig. 10 is explained by a mechanism that combines electrostatic interaction, hydrogen bonding, and π–π electrostatic attraction.

3.10.2. Effect of contact time. Fig. 11 illustrates the impact of contact time on the removal efficiency of RR-195, RB-222, and RB-5 dyes. Dye removal exhibits a significant increase during the initial phases of adsorption, thereafter transitioning to a slow approach to equilibrium for all three dyes. In the initial 0.5 hours, removal efficiencies of around 29%, 27% and 24% were attained for RR-195, RB-222 and RB-5, respectively, signifying the rapid occupation of the accessible active sites on the absorbent surface. A significant increase in dye adsorption was noted during 2 hours of contact time, with removal efficiencies of 53.8% (RR-195), 52.8% (RB-222) and 51.8% (RB-5). Subsequently, only a negligible increase in removal was seen, indicating saturation of the adsorption sites and the development of adsorption–desorption equilibrium. After 4 hours, the maximum removal efficiencies were approximately 56.5% for RR-195, 55.4% for RB-222, and 54.8% for RB-5. Among the examined dyes, RR-195 consistently showed marginally superior removal effectiveness at all contact durations, likely due to enhanced electrostatic interactions and a greater affinity of its functional groups for the adsorbent active sites.

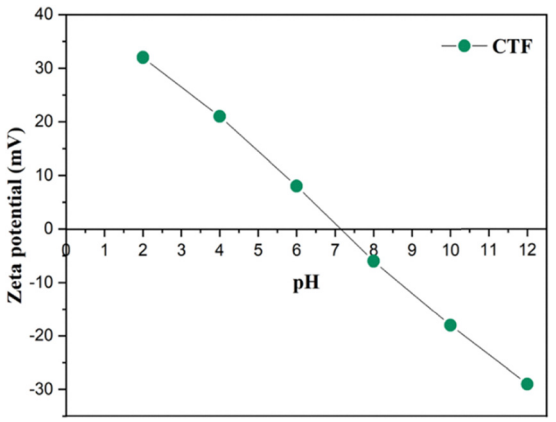

Fig. 10 Zeta potential analysis of the Fe_3O_4-adn-(1,3,5-triazine-2,4,6-triyl)triproline nanocomposite.

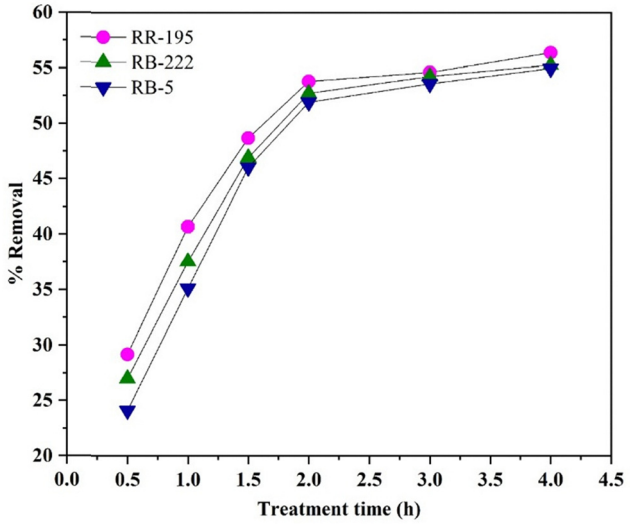

Fig. 11 Effect of treatment time on % dye removal of RR-195, RB-222 and RB-5 dyes by the Fe_3O_4-adn-(1,3,5-triazine-2,4,6-triyl)triproline nanocomposite (adsorbent dose = 10 mg, solution volume = 50 mL, solid–liquid ratio = 0.2 g L^{-1}, temperature = 298 K).

The same kinetic patterns exhibited by all dyes suggest that the adsorption process is predominantly regulated by surface-controlled interactions, characterized by fast initial uptake, followed by diffusion-limited equilibrium behavior.

3.10.3. Effect of the adsorbent dose on dye removal. Fig. 12 illustrates the impact of the adsorbent dosage on the removal efficiency of the dyes RR-195, RB-222, and RB-5. An increase in the adsorbent dosage from 10 to 50 mg led to a substantial improvement in dye removal, attributed to the augmented availability of active adsorbent sites. At a minimal dosage of 10 mg, the removal efficiencies were very low (about 28–33%), whereas at 50 mg, peak removal efficiencies of approximately 88–90% were attained. The fast rise in removal up to 30 mg adsorbent dosage signifies the efficient use of newly accessible surface sites, whereas the gradual increase beyond this threshold implies partial site saturation and diminished impetus for adsorption. RB-222 and RB-5 demonstrate marginally superior removal at elevated doses, while RR-195 exhibits relatively enhanced efficacy at lower doses.

3.10.4. Effect of the initial dye concentration. Fig. 13 illustrates the impact of the initial dye concentration on the removal of RR-195, RB-222, and RB-5 dyes. At low concentrations (5–15% w/v), removal efficiencies above 94% were noted for all dyes, demonstrating the adequate availability of active absorption sites. Optimal elimination occurred at a 10% (w/v) concentration, attaining 95.8% for RR-195, 95.0% for RB-222, and 94.6% for RB-5. A notable decline in the removal efficiency was seen with an increase in the dye concentration. At 40% (w/v) concentration, the removal efficiencies decreased to 48.5%, 45.0%, and 44.2% for RR-195, RB-222, and RB-5, respectively. The decrease is ascribed to the saturation of the adsorption sites and the high competition among the dye molecules at elevated concentrations. RR-195 consistently demonstrated marginally superior removal efficiency, indicating a greater affinity for the adsorbent surface. Minimal standard deviation values (SD $< 1\%$) indicated excellent experimental repeatability.

3.10.5. Kinetics modelling. The relationship between experimental data and theoretical kinetic models was established in order to gain a deeper understanding of the adsorption mechanism. By applying the pseudo-first-order (PFO) and pseudo-second-order (PSO) models, the kinetic behaviour of RR-195 sorption onto the Fe_3O_4-adn-(1,3,5-triazine-2,4,6-triyl)triproline nanocomposite was examined (Fig. 14). Eqn (3) and (4) are the linear equations for PFO and PSO, respectively, and Table 1 provides a summary of the fitting parameters.

$$\log(q_e - q_t) = \log q_e - \frac{k_1}{2.303} \times t \quad (3)$$

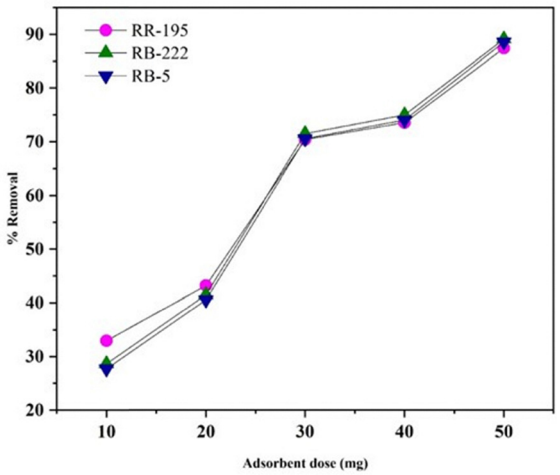

Fig. 12 Effect of adsorbent dosage on % dye removal of RR-195, RB-222 and RB-5 dyes by the Fe_3O_4-adn-(1,3,5-triazine-2,4,6-triyl)triproline nanocomposite (adsorbent dose = 10–50 mg, solution volume = 50 mL, solid–liquid ratio = 0.2–1.0 g L^{-1}, and temperature = 298 K).

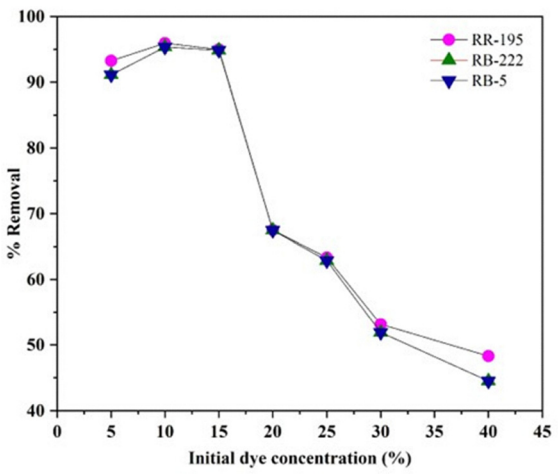

Fig. 13 Effect of initial dye concentration on % dye removal of RR-195, RB-222 and RB-5 dyes by the Fe_3O_4-adn-(1,3,5-triazine-2,4,6-triyl)triproline nanocomposite (adsorbent dose = 10 mg, solution volume = 50 mL, solid–liquid ratio = 0.2 g L^{-1}, and temperature = 298 K).

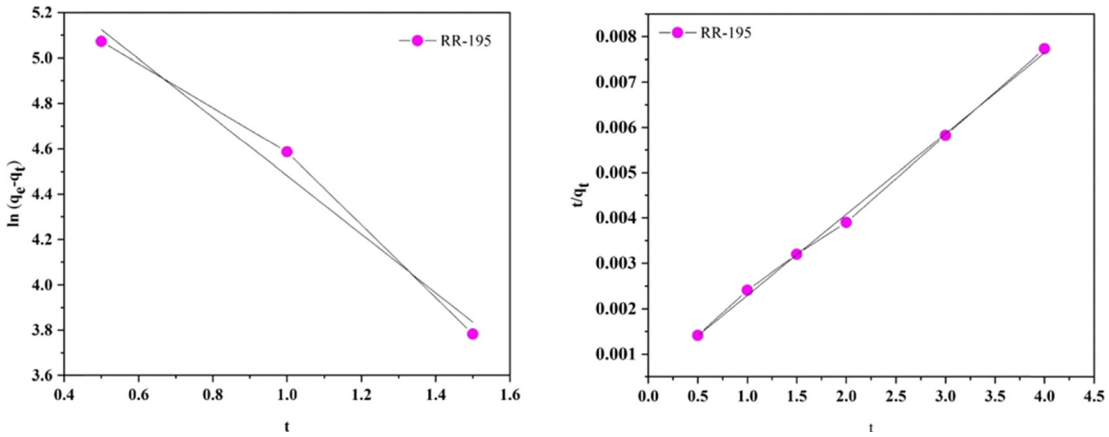

Fig. 14 Fitting curves of the RR-195 dye obtained from the pseudo-first-order and pseudo-second-order models.

Table 1 Kinetic parameters of the pseudo-first-order and pseudo-second-order models for the adsorption of the RR-195 dye onto the Fe_3O_4-adn-(1,3,5-triazine-2,4,6-triyl)triproline nanocomposite

	Pseudo first order			Pseudo second order		
Dye name	R^2	$q_{e,cal}$ (mg g^{-1})	k_1 (min^{-1})	R^2	$q_{e,cal}$ (mg g^{-1})	k_2 (min^{-1})
RR-195	0.9613	0.7612	1.30	0.9975	555.55	0.0063

$$\frac{t}{q_t} = \frac{1}{(k_2 \cdot q_e^2)} + \frac{1}{q_e} t \quad (4)$$

where the adsorption capabilities of the Fe_3O_4-adn-(1,3,5-triazine-2,4,6-triyl)triproline nanocomposite at equilibrium and at time t (min) are denoted by q_e (mg g^{-1}) and q_t (mg g^{-1}), respectively. In the pseudo-first-order kinetic model, the rate constant is denoted as k_1 (min^{-1}), whereas in the pseudo-second-order kinetic model, the equilibrium rate constant is represented by k_2 (g mg^{-1} min^{-1}). The PSO model proposes that chemisorption, which relies on the availability of binding sites, predominates, whereas the PFO model indicates diffusion as the rate-limiting step.

One important metric for assessing how well the model fits the experimental data is the correlation coefficient (R^2). In comparison to the PFO model, the PSO model showed a higher R^2 value (0.9975), and the computed q_e values were more in line with the experimental findings. These results suggest that chemisorption involving functional groups is primarily responsible for the adsorption of RR-195 onto the surface of the Fe_3O_4-adn-(1,3,5-triazine-2,4,6-triyl)triproline nanocomposite.

3.10.6. Adsorption isotherm modelling. To gain deeper insights into the equilibrium adsorption of RR-195 dye onto the Fe_3O_4-adn-(1,3,5-triazine-2,4,6-triyl)triproline nanocomposite, the experimental equilibrium data obtained from the concentration-dependent adsorption experiments (Fig. 15) were analysed using the Langmuir and Freundlich isotherm models. The nonlinear fitting results are presented in Fig. 15, and the corresponding isotherm parameters are summarized in Table 2.

The Langmuir isotherm model, which assumes monolayer adsorption on a homogeneous surface with a finite number of energetically equivalent adsorption sites, is expressed as follows:

$$q_e = \frac{q_{max} K_L C_e}{1 + K_L C_e}, \quad (5)$$

where q_e (mg g^{-1}) is the equilibrium adsorption capacity, q_{max} (mg g^{-1}) is the maximum monolayer adsorption capacity, K_L (L mg^{-1}) is the Langmuir constant related to the adsorption affinity, and C_e (mg L^{-1}) is the equilibrium dye concentration.

The Freundlich isotherm model, applicable to heterogeneous surfaces and multilayer adsorption, is expressed as follows:

$$q_e = K_F C_e^{1/n}, \quad (6)$$

where K_F is the Freundlich adsorption constant and $1/n$ represents the adsorption intensity.

The Langmuir model seems to fit the adsorption curve of the RR-195 dye better, with $R^2 > 0.99$, which indicates that the active sites are relatively homogeneously distributed and that adsorption occurs primarily through a monolayer (Table 2). This reflects the strong affinity of the dye molecules toward the Fe_3O_4-adn-(1,3,5-triazine-2,4,6-triyl)triproline nanocomposite.

3.10.7. Regeneration performance. The regeneration of the dye-loaded Fe_3O_4-adn-(1,3,5-triazine-2,4,6-triyl)triproline nanocomposite was evaluated under both acidic and alkaline conditions to restore its adsorption capacity. After adsorption, the nanocomposite was magnetically separated and stirred continuously for 60 minutes before being exposed to either 0.05 M HCl and 0.05 M NaOH. In an acidic medium, the protonation of triazine nitrogen and surface hydroxyl groups decreases the hydrogen bonding and electrostatic interactions, which encourages dye desorption. Conversely, alkaline treatment deprotonates surface functional groups, creating negatively charged sites that promote electrostatic repulsion with anionic dyes, such as Reactive Red 195. The regenerated adsorbent was magnetically recovered, neutralized to pH 7, dried at 70 °C, and

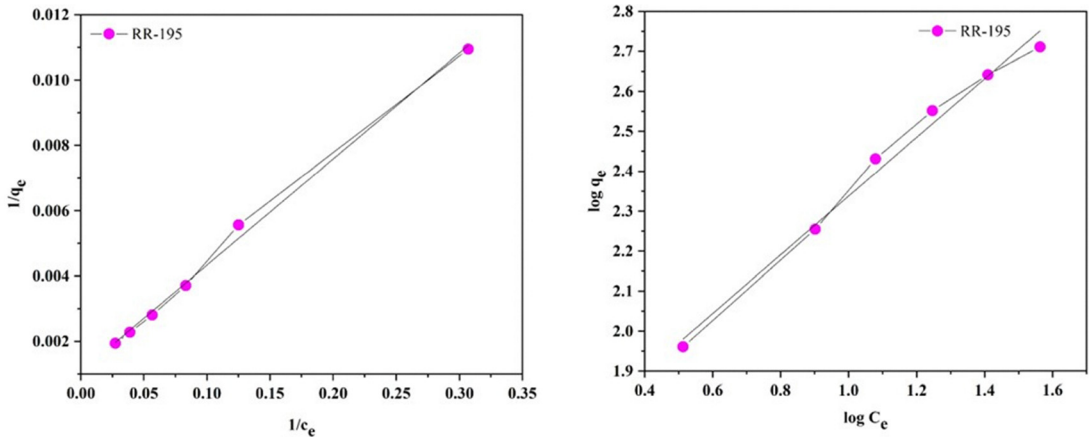

Fig. 15 Fitting curves of the RR-195 dye obtained from the Langmuir and Freundlich models.

Table 2 Langmuir and Freundlich isotherm parameters for the adsorption of the RR-195 dye onto the Fe_3O_4-adn-(1,3,5-triazine-2,4,6-triyl)triproline nanocomposite

	Langmuir isotherm			Freundlich isotherm		
Dye name	R^2	q_0	b	R^2	K_F	n
RR-195	0.9956	909.09	0.0338	0.9858	0.4724	0.3623

then used once more in subsequent adsorption cycles to show efficient and sustainable regeneration.

To investigate the stability and practical applicability, the reusability of the Fe_3O_4-adn-(1,3,5-triazine-2,4,6-triyl)triproline nanocomposite was examined in ten consecutive adsorption–desorption cycles. From Fig. 16, it can be observed that the adsorption capacity for RR-195 decreases gradually with increasing cycle number. After ten cycles, the remaining RR-195 adsorption capacity of the Fe_3O_4-adn-(1,3,5-triazine-2,4,6-triyl)triproline nanocomposite was more than ~65% of its initial value, showing good structural integrity and strong retention of active functional groups. The minor loss in adsorption performance could be due to the partial blockage of the active sites or incomplete desorption of residual dye molecules in the process of regeneration. Thus, according to these results, the synthesized structure possessed satisfactory reusability, confirming its potential for repeated use in the treatment of wastewater.

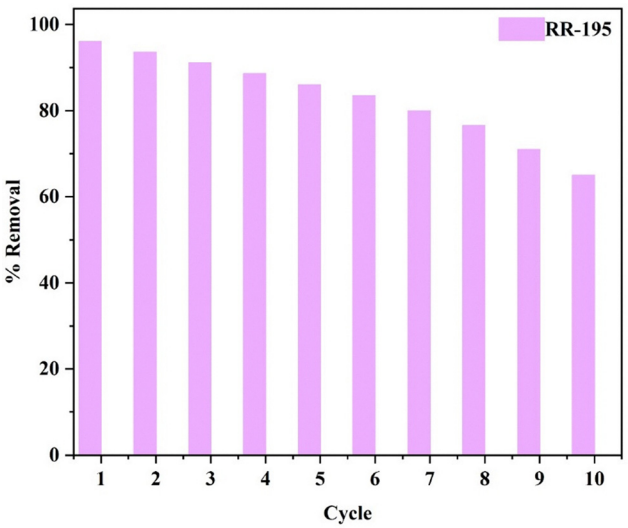

Fig. 16 Regeneration cycles.

3.10.8. Dye removal mechanism. The adsorption of the reactive dyes RR-195, RB-222, and RB-5 onto the triazine-modified magnetic polymeric network occurs *via* a synergistic, multi-interaction mechanism influenced by the surface chemistry of the adsorbent and the anionic characteristics of the dye molecules (Fig. 17). In acidic to near-neutral circumstances, the secondary amine groups from the proline units and exocyclic amine functional groups from adenine become protonated, resulting in a positively charged polymer surface. The protonation significantly increases the electrostatic interaction between the adsorbent and the sulfonate ($-SO_2$) groups of the reactive dyes, serving as the principal driving force for adsorption. Alongside electrostatic interactions, significant hydrogen bonding occurs between the –NH and –COOH groups within the polymeric structure and the azo (–N═N), sulfonate and heteroatom-containing moieties of the dye molecules. These interactions enhance adsorption stability and diminish dye desorption during agitation. Additionally, the π-conjugated s-triazine and adenine moieties facilitate π–π stacking and donor–acceptor interactions with the frameworks of the dyes. These interactions are especially important for large planar dye molecules such as RB-5 and RB-222, facilitating multilayer adsorption on the heterogeneous polymer surface. The cross-linked structure provides a high density of available functional sites, aligning with Freundlich-type adsorption characteristics.

Following dye adsorption, notable shifts and changes in the intensity of characteristic bands corresponding to Fe–O bonds (~580 cm^{-1}), triazine C═N vibrations (1500–1650 cm^{-1}), and –OH/–NH stretching (3200–3500 cm^{-1}) were noted. These spectral changes show that the surface functional groups are directly involved in the adsorption process. While changes in the triazine ring vibrations support π–π interactions between the adsorbent and aromatic dye molecules, the shift in the –OH/–NH bands suggests hydrogen bonding interactions.

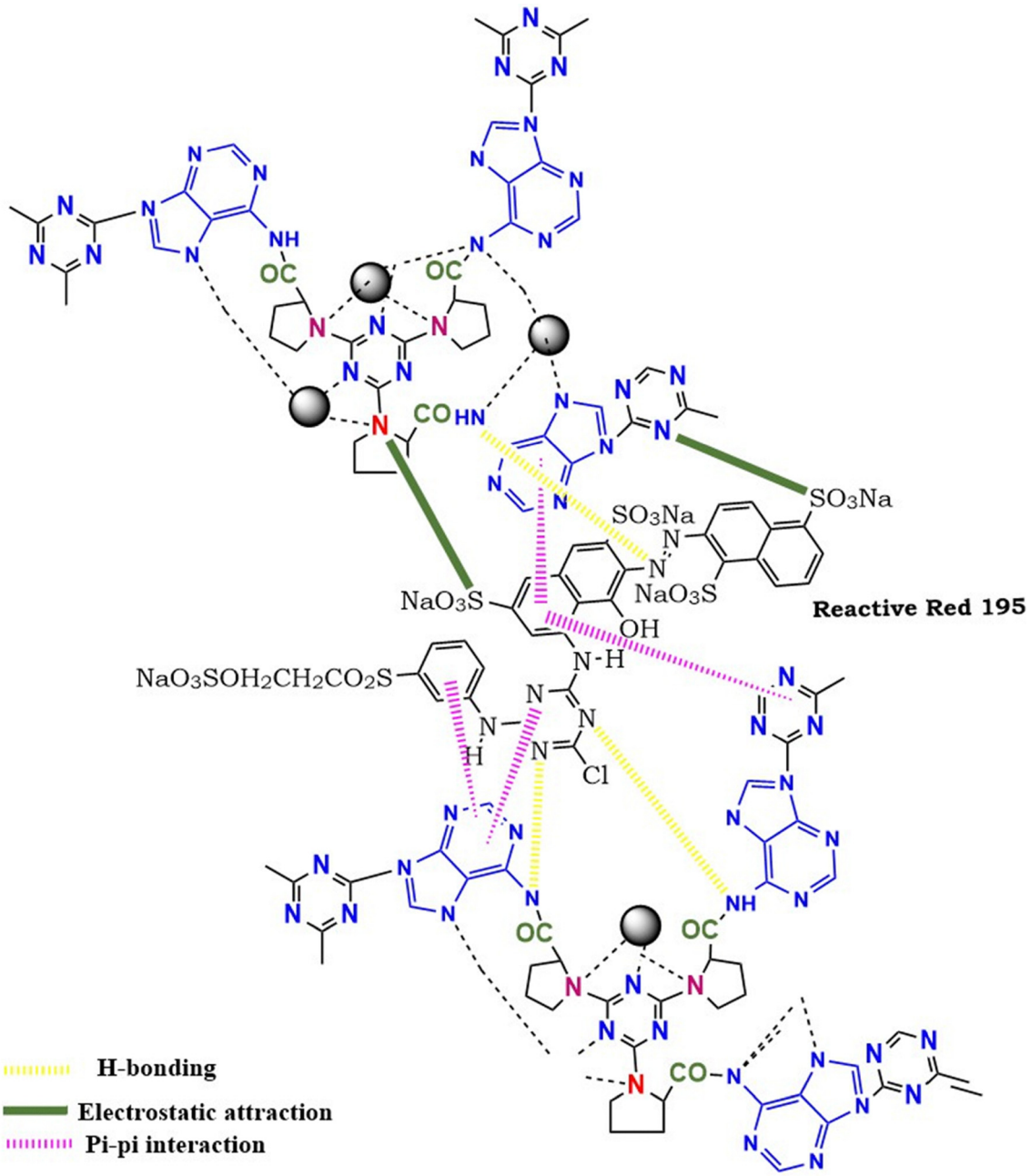

Fig. 17 Plausible interaction between the Fe_3O_4-adn-(1,3,5-triazine-2,4,6-triyl)triproline nanocomposite and the RR-195 dye molecule.

The main function of the Fe_3O_4 nanoparticles in the triazine-functionalised nanocomposite is to act as a magnetic core, which enables rapid magnetic separation and simple adsorbent recovery. Nonetheless, hydroxyl groups (–OH) are commonly found on the surface of Fe_3O_4 nanoparticles, and these groups may also take part in adsorption through weak coordination interaction or hydrogen bonding with dye molecules. However, the nitrogen-rich triazine functional groups provide the dominant adsorption sites and encourage strong interactions with reactive dyes through π–π interactions and electrostatic attraction. A multi-functional triazine-modified magnetic polymeric network facilitates the effective adsorption of reactive dyes *via* synergistic electrostatic, hydrogen bonding and π–π interactions, while incorporated Fe_3O_4 nano particles provide rapid magnetic separation and superior recyclability.

3.10.9. Comparative analysis of the adsorbents. Direct comparison of the adsorption efficiency among various adsorbents is frequently problematic due to large variations in experimental conditions, including pH, temperature, initial dye concentration, and contact duration across different investigations. Nonetheless, despite these discrepancies, a comparative evaluation of the adsorption capacities documented in the literature can yield significant insights. Table 3 displays a comparison of the highest adsorption capabilities of several

Table 3 Comparison of the recently reported magnetic triazine-based adsorbents and related Fe_3O_4 nanocomposites for dye removal from aqueous solutions

Sr. no.	Adsorbent	Target dye	Maximum adsorption capacity (mg g^{-1})	Ref.
1	CTF/Fe_2O_3	Methyl Orange	219	40
2	Magnetic covalent organic framework (Fe_3O_4@TpPDA)	Congo Red	179.4	41
3	Amino functionalised magnetic POP (FC-POP-EDA@Fe_3O_4)	Basic Red	379.75	42
4	Amino functionalised magnetic POP (FC-POP-EDA@Fe_3O_4)	Basic Blue 41	240.9	42
5	Fe_3O_4@tannic acid@ZIF-67	Cd(II)	215.5	43
6	Fe_3O_4@tannic acid@ZIF-67	Mn(II)	138.9	43
7	Phenolate-rich anionic covalent organic frameworks	Basic Green 1	302.70	44
8	Phenolate-rich anionic covalent organic frameworks	Methylene Blue	279.97	44
9	Fe_3O_4-adn-(1,3,5-triazine-2,4,6-triyl)triproline nanocomposite	Reactive Red 195	909.9	Present study

reported adsorbents for the removal of the RR-195 dye. The Fe_3O_4-adn-(1,3,5-triazine-2,4,6-triyl)triproline nanocomposite synthesised in this study exhibits superior performance compared to several previously reported materials, affirming its high affinity and efficiency for the removal of dye from aqueous environments.

4. Conclusion

Herein, we successfully prepared a Fe_3O_4-adn-(1,3,5-triazine-2,4,6-triyl)triproline nanocomposite that functions effectively as an adsorbent for removing dyes from industrial wastewater and can be recovered magnetically. Structural and surface characterization indicated that triazine moieties were well anchored to the Fe_3O_4 core, creating a stable hybrid framework with nitrogen-containing active sites. The nanocomposite retained its super magnetic properties, facilitating easy and rapid magnetic separation after dye adsorption. Adsorption tests showed that industrial reactive dyes were efficiently removed. This was achieved through a combination of electrostatic interactions, π–π stacking, hydrogen bonding, and surface complexation. Kinetic and isotherm investigations demonstrated a chemisorption-dominated process on the homogeneous surface, indicating monolayer adsorption characterised by dye-adsorbent interaction. The nanocomposite demonstrated excellent recyclability, maintaining a high adsorption capacity across multiple regeneration cycles with minimal loss of performance. It is very efficient can be separated by magnets, and structurally stable shows that is might be used again and again. In general, the covalent triazine-capped Fe_3O_4 nanocomposite is a robust and durable adsorbent for cleaning up dyes. The mechanistic insights and reusability exhibited in this study provide a valuable basis for the development of improved magnetic nanoparticles for effective wastewater treatment applications.

Conflicts of interest

The authors declare that they have no known competing financial interest or personal relationships that could have appeared to influence the work reported in this paper.

Data availability

The datasets generated/analyzed during the current study are included within this article.

Supplementary information (SI) is available. See DOI: https://doi.org/10.1039/d6ma00006a.

References

1 T. E. Oladimeji, M. Oyedemi, M. E. Emetere, O. Agboola, J. B. Adeoye and O. A. Odunlami, Review on the impact of heavy metals from industrial wastewater effluent and removal technologies, *Heliyon*, 2024, **10**(23), e40370, DOI: 10.1016/j.heliyon.2024.e40370.
2 K. F. Kayani, Bimetallic metal–organic frameworks (BMOFs) for dye removal: a review, *RSC Adv.*, 2024, **14**(43), 31777–31796, DOI: 10.1039/D4RA06626J.
3 Ö. Gökkuş, E. Brillas and I. Sirés, Sequential use of a continuous-flow electrocoagulation reactor and a (photo) electro-Fenton recirculation system for the treatment of Acid Brown 14 diazo dye, *Sci. Total Environ.*, 2024, **912**, 169143, DOI: 10.1016/j.scitotenv.2023.169143.
4 Ö. Gökkuş and M. Oğuz, Investigation of color and COD removal by Fenton reagent from aqueous solutions containing acid and reactive dyestuffs, *Desalin. Water Treat.*, 2011, **26**(1–3), 160–164, DOI: 10.5004/dwt.2011.2119.
5 P. V. Nidheesh and Ö. Gökkuş, Aerated iron electrocoagulation process as an emerging treatment method for natural water and wastewater, *Sep. Sci. Technol.*, 2023, **58**(11), 2041–2063, DOI: 10.1080/01496395.2023.2227913.
6 F. Uddin, Environmental hazard in textile dyeing wastewater from local textile industry, *Cellulose*, 2021, **28**(17), 10715–10739, DOI: 10.1007/s10570-021-04228-4.
7 B. Lellis, C. Z. Fávaro-Polonio, J. A. Pamphile and J. C. Polonio, Effects of textile dyes on health and the environment and bioremediation potential of living organisms, *Biotechnol. Res. Innovation*, 2019, **3**(2), 275–290, DOI: 10.1016/j.biori.2019.09.001.
8 B. Ghosh, R. Saha, D. Bhattacharya and M. Mukhopadhyay, Laccase and its source of sustainability in an enzymatic biofuel cell, *Bioresour. Technol. Rep.*, 2019, **6**, 268–278, DOI: 10.1016/j.biteb.2019.03.013.

9 N. Hemashenpagam and S. Selvajeyanthi, Textile dyes and their effect on human beings, *Nanohybrid materials for treatment of textiles dyes*, Springer Nature Singapore, Singapore, 2023, pp. 41–60, DOI: 10.1007/978-981-99-3901-5_3.
10 P. Mani, V. T. Fidal, T. Keshavarz, T. S. Chandra and G. Kyazze, Laccase immobilization strategies for application as a cathode catalyst in microbial fuel cells for azo dye decolourization, *Front. Microbiol.*, 2021, **11**, 620075, DOI: 10.3389/fmicb.2020.620075.
11 S. Ben Younes, I. Cherif, A. Dhouib and S. Sayadi, Trametes trogii: a biologic powerful tool for dyes decolorization and detoxification, *Catal. Lett.*, 2016, **146**(1), 204–211, DOI: 10.1007/s10562-015-1629-x.
12 H. Zouari-Mechichi, T. Mechichi, A. Dhouib, S. Sayadi, A. T. Martínez and M. J. Martinez, Laccase purification and characterization from Trametes trogii isolated in Tunisia: decolorization of textile dyes by the purified enzyme, *Enzyme Microb. Technol.*, 2006, **39**(1), 141–148, DOI: 10.1016/j.enzmictec.2005.11.027.
13 U. Chadha, S. K. Selvaraj, S. V. Thanu, V. Cholapadath, A. M. Abraham, M. Manoharan and V. Paramsivam, A review of the function of using carbon nanomaterials in membrane filtration for contaminant removal from wastewater, *Mater. Res. Express*, 2022, **9**(1), 012003, DOI: 10.1088/2053-1591/ac48b8.
14 S. R. Patel, I. R. Patel, N. H. Patel and B. V. Patel, Microwave-assisted fabrication for synthesis of magnetite chitosan-modified polymer composite hydrogel as rapid removal adsorbent for effective remediation of hazardous contaminants, *Polym. Bull.*, 2024, **81**(1), 449–473, DOI: 10.1007/s00289-023-04721-9.
15 Y. Li, Y. An, R. Zhao, Y. Zhong, S. Long, J. Yang and H. Zheng, Synergetic removal of oppositely charged dyes by co-precipitation and amphoteric self-floating capturer: mechanism investigation by molecular simulation, *Chemosphere*, 2022, **296**, 134033, DOI: 10.1016/j.chemosphere.2022.134033.
16 S. R. Bharucha, M. S. Dave, S. H. Chaki and T. A. Limbani, Thermal investigation of $NbSe_2$ nanoparticles synthesized through a temperature-dependent sonochemical method, *RSC Adv.*, 2024, **14**(45), 33459–33470, DOI: 10.1039/D4RA05108D.
17 D. Pan, Y. Song, C. Liu and Z. Guo, Research progress on wastewater treatment in food industry: a mini-review, *ES Food Agrofor.*, 2022, **10**(2), 10–23, DOI: 10.30919/esfaf793.
18 S. Soni, P. K. Bajpai, J. Mittal and C. Arora, Utilisation of cobalt doped Iron based MOF for enhanced removal and recovery of methylene blue dye from waste water, *J. Mol. Liq.*, 2020, **314**, 113642, DOI: 10.1016/j.molliq.2020.113642.
19 A. Afkhami and R. Moosavi, Adsorptive removal of Congo red, a carcinogenic textile dye, from aqueous solutions by maghemite nanoparticles, *J. Hazard. Mater.*, 2010, **174**(1–3), 398–403, DOI: 10.1016/j.jhazmat.2009.09.066.
20 S. Qadri, A. Ganoe and Y. Haik, Removal and recovery of acridine orange from solutions by use of magnetic nanoparticles, *J. Hazard. Mater.*, 2009, **169**(1–3), 318–323, DOI: 10.1016/j.jhazmat.2009.03.103.
21 L. Zhou, C. Gao and W. Xu, Magnetic dendritic materials for highly efficient adsorption of dyes and drugs, *ACS Appl. Mater. Interfaces*, 2010, **2**(5), 1483–1491, DOI: 10.1021/am100114f.
22 S. Y. Mak and D. H. Chen, Fast adsorption of methylene blue on polyacrylic acid-bound iron oxide magnetic nanoparticles, *Dyes Pigm.*, 2004, **61**(1), 93–98, DOI: 10.1016/j.dyepig.2003.10.008.
23 D. W. Wang, F. Li, G. Q. Lu and H. M. Cheng, Synthesis and dye separation performance of ferromagnetic hierarchical porous carbon, *Carbon*, 2008, **46**(12), 1593–1599, DOI: 10.1016/j.carbon.2008.06.052.
24 N. Yang, S. Zhu, D. Zhang and S. Xu, Synthesis and properties of magnetic Fe3O4-activated carbon nanocomposite particles for dye removal, *Mater. Lett.*, 2008, **62**(4–5), 645–647, DOI: 10.1016/j.matlet.2007.06.049.
25 L. C. Oliveira, R. V. Rios, J. D. Fabris, V. Garg, K. Sapag and R. M. Lago, Activated carbon/iron oxide magnetic composites for the adsorption of contaminants in water, *Carbon*, 2002, **40**(12), 2177–2183, DOI: 10.1016/S0008-6223(02)00076-3.
26 L. Ai, H. Huang, Z. Chen, X. Wei and J. Jiang, Activated carbon/$CoFe_2O_4$ composites: facile synthesis, magnetic performance and their potential application for the removal of malachite green from water, *Chem. Eng. J.*, 2010, **156**(2), 243–249, DOI: 10.1016/j.cej.2009.08.028.
27 M. Ejaz, M. G. Mohamed, M. G. Kotp, A. M. Elewa and S. W. Kuo, Triphenylamine-linked triazine (DA) units based hypercrosslinked porous polymer: rapid adsorption and enhanced photodegradation of organic dyes from water, *Colloids Surf., A*, 2025, 137239, DOI: 10.1016/j.colsurfa.2025.137239.
28 S. S. Shafqat, S. H. Sumrra, M. N. Zafar, S. Aslam, M. I. Vohra, M. Nosheen and M. A. Khan, Modification of amino functionalized silica nanoparticles with L-proline and furanacrylic acid as novel composites for the efficient removal of methyl orange, *Mater. Today Commun.*, 2024, **39**, 108934, DOI: 10.1016/j.mtcomm.2024.108934.
29 I. Ahmad, A. Abbasi, Z. M. El Bahy and S. Ikram, Synergistic effect of silver NPs immobilized on Fe_3O_4@ L-proline magnetic nanocomposite toward the photocatalytic degradation of Victoria blue and reduction of organic pollutants, *Environ. Sci. Pollut. Res.*, 2023, **30**(32), 78891–78912, DOI: 10.1007/s11356-023-27837-x.
30 A. Maleki and R. Firouzi-Haji, L-proline functionalized magnetic nanoparticles: a novel magnetically reusable nanocatalyst for one-pot synthesis of 2,4,6-triarylpyridines, *Sci. Rep.*, 2018, **8**(1), 17303, DOI: 10.1038/s41598-018-35676-x.
31 J. Wu, J. Liu, B. Wen, Y. Li, B. Zhou, Z. Wang and R. Zhao, Nitrogen-rich covalent triazine frameworks for high-efficient removal of anion dyes and the synergistic adsorption of cationic dyes, *Chemosphere*, 2021, **272**, 129622, DOI: 10.1016/j.chemosphere.2021.129622.
32 F. Ahmadijokani, S. Ahmadipouya, M. H. Haris, M. Rezakazemi, A. Bokhari, H. Molavi and M. Arjmand, Magnetic nitrogen-rich UiO-66 metal–organic framework: an efficient adsorbent for water treatment, *ACS Appl. Mater. Interfaces*, 2023, **15**(25), 30106–30116, DOI: 10.1021/acsami.3c02171.

33 S. E. Peter, A. Bera, S. R. Vennapusa, P. Vairavel and N. V. A. Kumar, From Computational Screening to Enhanced Adsorption: Optimized Removal of Toxic Congo Red by Nitrogen-rich Triazine Polymers, *Macromol. Mater. Eng.*, 2025, e00366, DOI: 10.1002/mame.202500366.

34 Divya, S. Kalla and R. Jangir, Azo-linked nanoporous organic polymer for efficient capture of cationic dyes and radioactive iodine, *J. Mater. Sci.*, 2025, 1–22, DOI: 10.1007/s10853-025-11816-3.

35 S. Abolghasemi, A. Nasiri, M. Hashemi, S. Rajabi and F. Rahimi, Magnetic nanocomposites: innovative adsorbents for antibiotics removal from aqueous environments–a narrative review, *Appl. Water Sci.*, 2025, **15**(2), 30, DOI: 10.1007/s13201-025-02360-1.

36 A. Mehmood, F. S. A. Khan, N. M. Mubarak, Y. H. Tan, R. R. Karri, M. Khalid and S. A. Mazari, Magnetic nanocomposites for sustainable water purification—a comprehensive review, *Environ. Sci. Pollut. Res.*, 2021, **28**(16), 19563–19588, DOI: 10.1007/s11356-021-12589-3.

37 L. S. Rocha, É. M. Sousa, D. Pereira, M. V. Gil, G. Otero-Irurueta, M. J. H. Gallo and V. Calisto, Sustainable and recoverable waste-based magnetic nanocomposites used for the removal of pharmaceuticals from wastewater, *Chem. Eng. J.*, 2021, **426**, 129974, DOI: 10.1016/j.cej.2021.129974.

38 D. Yadav and S. K. Awasthi, Recent advances in the design, synthesis and catalytic applications of triazine-based covalent organic polymers, *Mater. Chem. Front.*, 2022, **6**(12), 1574–1605, DOI: 10.1039/D2QM00071G.

39 M. E. Peralta, S. Ocampo, I. G. Funes, F. Onaga Medina, M. E. Parolo and L. Carlos, Nanomaterials with tailored magnetic properties as adsorbents of organic pollutants from wastewaters, *Inorganics*, 2020, **8**(4), 24, DOI: 10.3390/inorganics8040024.

40 W. Zhang, F. Liang, C. Li, L. G. Qiu, Y. P. Yuan, F. M. Peng and J. F. Zhu, Microwave-enhanced synthesis of magnetic porous covalent triazine-based framework composites for fast separation of organic dye from aqueous solution, *J. Hazard. Mater.*, 2011, **186**(2–3), 984–990, DOI: 10.1016/j.jhazmat.2010.11.093.

41 S. Lu, Y. Wei, S. Long, Z. Chen, F. Chen, H. Lin and J. Lu, Efficient adsorption and removal of congo red from aqueous solution using magnetic covalent organic framework nanocomposites, *ChemistrySelect*, 2023, **8**(1), e202203621, DOI: 10.1002/slct.202203621.

42 N. Taheri and M. Dinari, Amino-functionalized magnetic porous organic polymer for the selective removal of toxic cationic dyes from textile wastewater, *New J. Chem.*, 2022, **46**(23), 11174–11184, DOI: 10.1039/D2NJ01754G.

43 J. Wu, Z. Xiang, Y. Li, J. Lv and X. Peng, PSS-Functionalized Fe_3O_4/ZIF-67 Nanocomposite: An Efficient Adsorbent for Rapid Removal of Microplastics From Wastewater, *ChemistrySelect*, 2026, **11**(6), e06885, DOI: 10.1002/slct.202506885.

44 M. Nozaki, T. Irie, K. Sasaki, S. Sasikumar, T. Kawawaki, H. Maricherla and Y. Negishi, Phenolate-Rich Anionic Covalent Organic Frameworks with Engineered Reticular Microenvironments Enable Selective Dye Capture from Model Solutions and Real Textile Wastewater, 2026, DOI: 10.26434/chemrxiv.15000563/v1.